Materials Research Express

PAPER

Predicted bandgap opening in highly-oriented wrinkles formed in chemical vapour deposition grown graphene

To cite this article: Omar M Dawood *et al* 2019 *Mater. Res. Express* **6** 026311

Materials Research Express

PAPER

Predicted bandgap opening in highly-oriented wrinkles formed in chemical vapour deposition grown graphene

RECEIVED
23 October 2018

REVISED
1 November 2018

ACCEPTED FOR PUBLICATION
14 November 2018

PUBLISHED
28 November 2018

Omar M Dawood[1,2,3], **Rakesh K Gupta**[1,4], **Faisal H Alqahtani**[1,5], **Umberto Monteverde**[1], **Hong-Yeol Kim**[1], **James Sexton**[1], **Liam Britnell**[6], **Robert J Young**[2,6], **Nigel W Hodson**[7], **Mohamed Missous**[1] and **Max A Migliorato**[1,8]

[1] School of Electrical and Electronic Engineering, University of Manchester, United Kingdom
[2] School of Materials, University of Manchester, United Kingdom
[3] Department of Physics, College of Education for Pure Science, University of Anbar, Anbar, Iraq
[4] Manchester Institute of Biotechnology, University of Manchester, United Kingdom
[5] King Khalid University, Abha, Saudi Arabia
[6] National Graphene Institute, University of Manchester, United Kingdom
[7] BioAFM Facility, Faculty of Biology, Medicine and Health, University of Manchester, United Kingdom
[8] Author to whom any correspondence should be addressed

Keywords: Raman spectroscopy, AFM, DFT

Supplementary material for this article is available online

Abstract

We present a combined atomic force microscopy and Raman spectroscopy study of wrinkle formation in chemical vapour deposition graphene. Graphene was grown on copper and repeatedly transferred onto a SiO_2 substrate to form a four-layer graphene stack. By means of depositing two electrodes with a small gap of 1 μm on top of graphene, we can generate a long wrinkle along the channel. Such a wrinkle is pronounced and seems to form at the expense of other wrinkles otherwise present. Along the wrinkle, the strain measured by both atomic force microscopy and polarized Raman is revealed to be of a biaxial type, which is shown, through atomistic modelling, is predicted to produce a sizeable bandgap opening of up to 0.4 eV. Since graphene is normally a zero bandgap material, its applications as an electronic material for devices can be limited. The approach presented in this work could lead to graphene exhibiting a controllable bandgap similar to a semiconductor material that could, therefore, be exploited for the fabrication of graphene-based electronic devices.

1. Introduction

Large area chemical vapor deposition (CVD) graphene is an essential enabler for realizing the translation from prototype to fully mass-producible graphene-based electronic devices [1, 2]. Already large sizes (several cm^2) of monolayer graphene can be synthesized on an inexpensive substrate, such as copper, albeit quality control issues still exist e.g. graphene is generally grown on polycrystalline copper, resulting in a large number of nucleation sites which, as the domains increase in size, coalesce into a film comprising a large number of grain boundaries and point defects detrimental to material performance [3, 4]. Further to its monolayer form, multilayer CVD graphene, with improved electrical conductivity, has potential as e.g. a replacement for Indium Tin Oxide (ITO) for transparent electrodes [5, 6], or as gate material in transistors [7]. In this work, we show how the device fabrication process can also be exploited to add further functionality to the CVD graphene films, by exploiting strain generated during the metal electrodes deposition to tune the electronic properties of multilayered graphene films transferred onto the SiO_2 and generate an exploitable electronic bandgap in the otherwise zero-bandgap graphene films. It is wothwhile to mention that the work presented in the current article has been motivated from the results obtained and predictions formed from studies in past [8–12]. Most of these studies were not aimed to create a strained ripple whilst stacking graphene films one on other until a uniform and reproducible strained graphene ripple is formed as presented in our article. For instance, the articles suggested by [11] present studies on wrinkles and ripples formed naturally/randomly whilst transfer of CVD graphene

through conventional polymer based transfer, due to different thermal expansion of graphene and substrate, wrinkles in exfoliated graphene etc. Since, band-gap opening has been predicted by many studies in highly oriented graphene, the aim of our article is to prove it experimentally that a uniform strained graphene ripple can be produce through the methods described in the article and rigorously analysis of AFM maps and Raman spectra predicts the band-gap opening in strained graphene.

2. Experimental procedures

2.1. Morphology

Evaporated Au/Ti electrodes were deposited on four-layer graphene with separations varying between 1 μm to 10 μm. Details of the fabrication method are given in the section 1 in supplementary information is available online at stacks.iop.org/MRX/6/026311/mmedia. To analyze the morphology of such layers and their dependence on the size of the separation between the electrodes AFM images were recorded of the graphene regions between the contacts. The systems and setting used for the AFM measurements are mentioned in section 1 in the supplementary information.

The region with a 10 μm gap is shown in figure 1. Bright lines of varying heights decorate the graphene surface. As evident from figures 1(a)–(c), the orientations of these lines are randomly distributed, forming domains of different sizes. These bright lines are wrinkles that originate from out-of-plane distortion of the graphene surface. Such wrinkles in CVD graphene tend to form along grain boundaries [13–15], where the carbon atoms are weakly bonded and able to respond quickly to any external perturbation.

The cross-sections of the height profiles along three lines orthogonal to the electrodes, (figure 1(a)) reveal that the height/width of these wrinkles ranges from 3/140 nm to 35/480 nm. The heights and widths appear to be inversely related, which suggests that the volume of space under the features is roughly constant. Given that the top layer of graphene is separated from the substrate by a further three layers, it is unlikely that these features originate directly from interaction with the substrate.

For comparison, three-layer and a monolayer graphene equivalent control samples (supplementary information figure SI1) were analysed to further legitimizing the assumption that the substrate effect decays as the number of layers increases. It is also inferred that the top layer is more prone to surface perturbations and as a result is more pliable, with the wrinkles, resulting from the deformation induced by the electrodes themselves. It is worth mentioning that no substantial wrinkles were found in areas away from the electrodes in the four-layer graphene case.

In previous work [16], it was shown that the different amounts of strain for four-layer graphene could be associated with different supporting materials used; SiO_2 or GaAs. The origin of the stress was assumed to be from underneath the graphene layer upon interacting with the substrate surface and then transferred onto the topmost graphene layer. Here instead, it appears that an even stronger source of strain comes from the deposited top electrodes, either from thermal shrinking upon cooling or the weight of the metal itself. Such strain should be expected to decay away from the electrodes. If such an assumption is correct then when the electrode separation is reduced to 1 μm, such a decay should be lower, resulting in a higher strain. As a result higher height features should be observed. This is indeed the case, as shown in figure 2. Rather than wrinkles appearing with random orientations, a long, regular and substantially sized wrinkle forms along the boundaries of the electrodes, roughly in the middle of the channel. Moreover, the continuity in the formation of this wrinkle has spread beyond the end of the electrodes. This observation is similar to that made by Shioya *et al* [17], where thermal shrinking was identified as the cause for the ripple forming.

To further study and elaborate, four lines were selected (figure 2(a)). For line 1, as shown in figures 2(c)–(d), the height and width of the wrinkles are 26 nm and 268 nm, respectively. For line 2, sketched in a different area, there is a significant change in the height and width of the wrinkle (51 nm and 140 nm, respectively). Data from this line is not presented in figure 2 as it is analyzed in detail in the following section. For line 3, figures 2(e)–(f), the height is less than 10 nm and is hence a minor break in the continuity of the wrinkle, which can be considered as a defect. For line 4, the height of the wrinkle, figures 2(g)–(h), is about 72 nm and its width is 217 nm. This analysis shows that though the wrinkle appears regular, on close inspection height variations ranging from 10 nm to 72 nm are present, with occasional defects with reduced height.

The principle behind wrinkle formation in graphene is similar to what happens to soap bubbles when they come in contact. Under the influence of an external pressure with a specific direction, these bubbles will coalescence to form a single larger bubble. If the same principle is adopted for graphene, islands of wrinkles, as shown in the inset graph of figure 1(b) for the 10 μm channel, will coalesce due to the large exerted stress by the electrodes, thus forming a single linear wrinkle with distinct topographical properties as shown in figure 2(b) for the 1 μm channel.

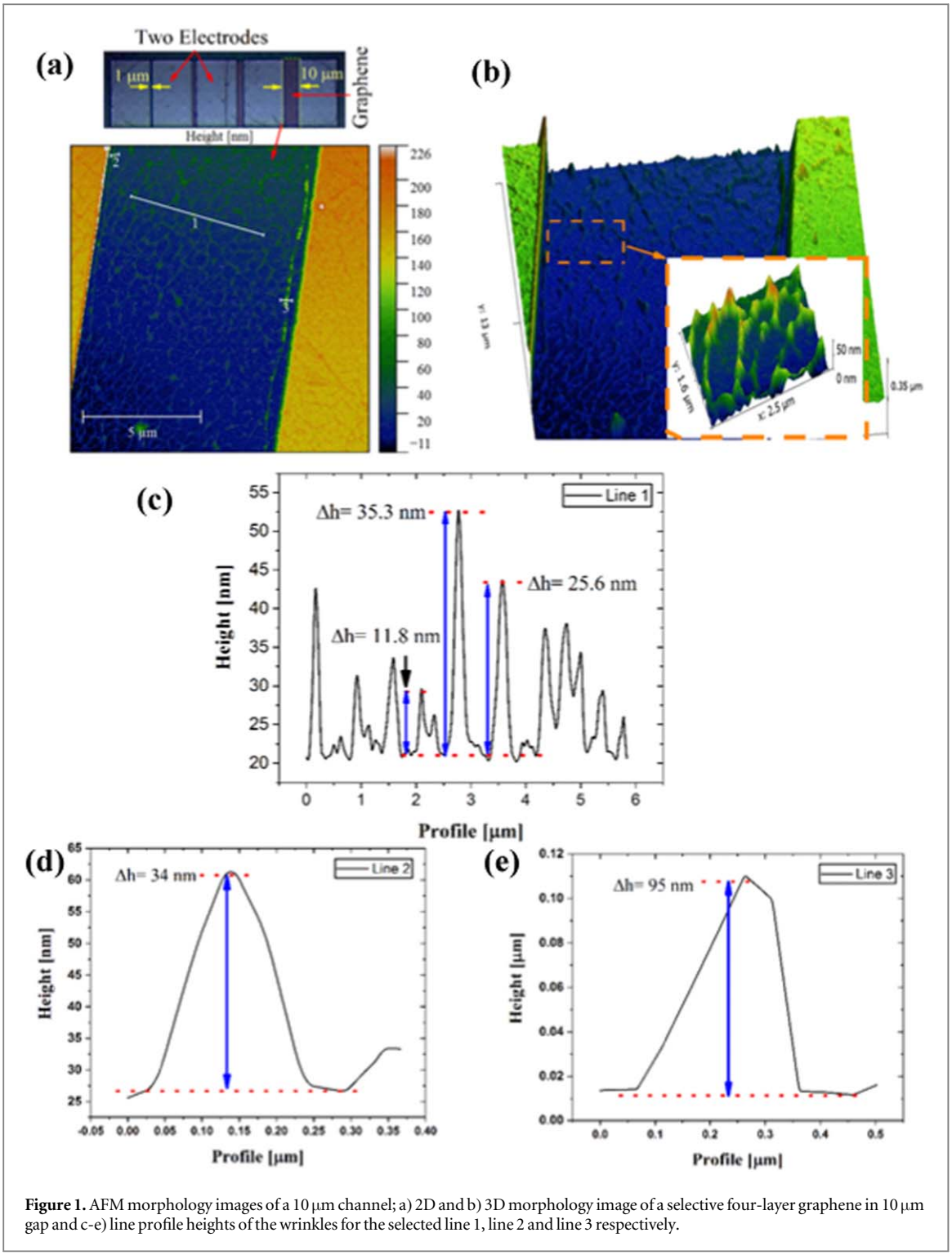

Figure 1. AFM morphology images of a 10 μm channel; a) 2D and b) 3D morphology image of a selective four-layer graphene in 10 μm gap and c-e) line profile heights of the wrinkles for the selected line 1, line 2 and line 3 respectively.

Two aspects are crucial. The first one is the bending rigidity of graphene, which occurs as a result of the out-of-plane deformation of monolayer graphene. Its value depends on the number of graphene layers [18]. The second one is the interlayer shear interaction, which has a considerable impact on the value of the bending rigidity and is the reason for adjacent graphene layers to slide over each other under the influence of external deformation. Increasing the number of graphene layers will reduce interlayer shear interaction and thus accelerate the sliding of the graphene layers while increasing to buckling of the graphene layer [19]. Sliding the topmost graphene layer starts at the edge of the two electrodes where a large amount of compressive stress is predicted, whereas a single wrinkle can be produced in the middle of the 1 μm channel [20].

The morphological features observed are repeatable. Several structures were observed to have the same wrinkle formation when the separation between the electrodes is lower than 3 μm (see SI section 5). In terms of uniformity, figure 3 shows a statistical correlation between heights and widths of the wrinkles. 180

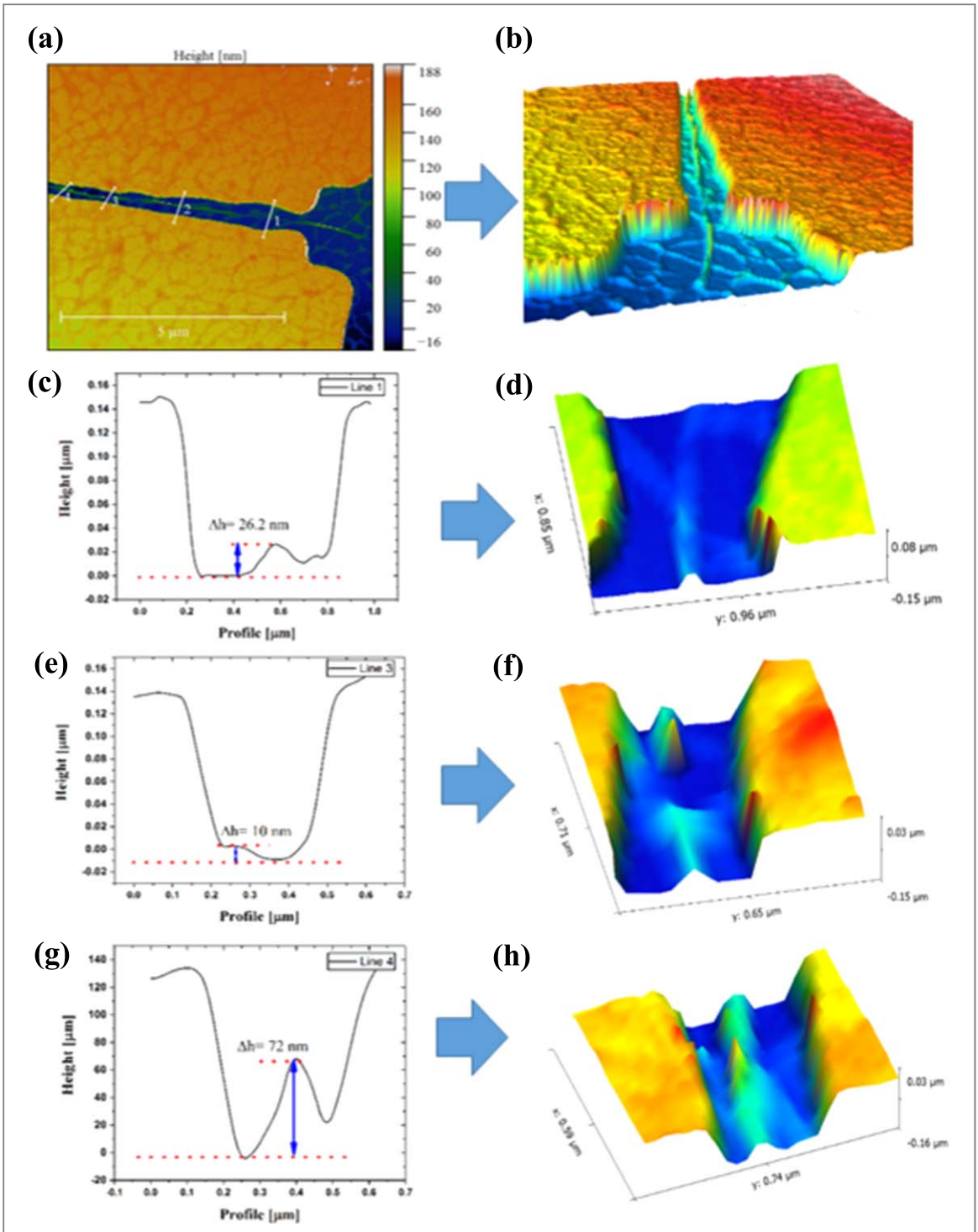

Figure 2. a) AFM morphology images of a 1 µm channel; a) 2D and b) 3D morphology images of the four-layer graphene in the 1 µm gap and c-h) line profiles heights with associated 3D image of the wrinkles for the selected line 1, line 3 and line 4 respectively.

measurements were taken from 12 separate structures. The combination of height and width is not random and by fitting a line, it reported that the height is usually 40% of the width, with the great proportion of data points appearing to aggregate in the range 10 nm to 30 nm or the height and 100 nm–200 nm for the width. Notably, ripples do appear in three layers systems. However, the case of 3 layers, the orientation of these winkles is random not aligned in one direction. Whereas, with 4 layers, wrinkles were more aligned along the 1 um gap between the two contacts as presented in figure SI.8 in the supplementary information. Once, it was confirmed, after the repeated fabrication of several devices, that with four layers of graphene a strained wrinkle/ripple could be formed with high reproducibility. We did not explore with five or more layers. The idea of forming a strained ripple and possibility of opening band gap is now been explored on a dielectric layer, instead of stack of graphene

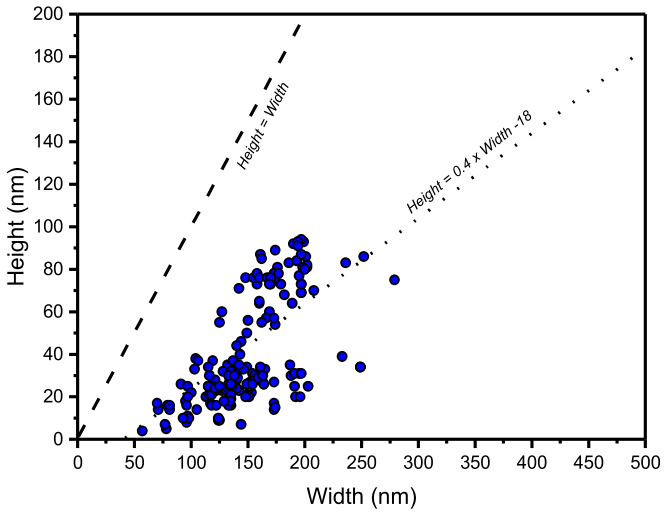

Figure 3. Statistical correlation between heights and widths of the wrinkles. 180 measurements were taken from 12 separate structures. The fitted line shows that the height is usually 40% of the width.

layers. This could be useful to conduct electrical studies to prove electrically the opening of band gap useful to make switching devices, which shall be published in future articles elsewhere.

2.2. Raman spectroscopy

Raman spectroscopy was used to determine whether the optical properties of the top layer of graphene can be analyzed separately from those of the underlying layers. Raman spectroscopy is often used to detect the number of graphene layers [21], their crystalline structure, i.e. the presence of defects [22], the concentration of negative or positive dopants [23, 24], and the presence/absence of stress [15, 25]. Furthermore, the Raman polarisation measurements can also reveal the presence of different types of stress [26, 27].

Figure 4 shows the results for; (a) metallized sample with (b) 10 μm and (c) 1 μm gaps, at four distinct points (figure 4(a), points 1 to 4) along the channel, between the electrodes. Differences in the Raman spectra can be associated with variations in the patterns of stacking between the four layers of graphene following the discussion in [16]. According to such interpretation, the difference in the Raman spectrum of figure 4(b) for the 10 μm channel (points 1 to 4), would originate from multilayer graphene having Bernal interlayer stacking (ABA stacking), turbostratic interlayer stacking (an arbitrary angle between layers) or twisted interlayer stacking (at a specific angle between layers). The different stacking patterns have a varying degree of interlayer interaction, that is reflected in the Raman spectra (more with respect to the 2D mode than the G mode). It is worth mentioning here that having found one instance of Bernal stacking is an extremely lucky coincidence and in fact a rare one. Most measurements shown in section 5 in supplementeray information typically reflect the presence of random or turbostratic stacking.

In general, the interaction between graphene layers is most intense when a short-range order is achieved e.g ABA stacking, and reduced when the long-range order is present, e.g. when layers are randomly oriented (twisted) at an angle between each other [21, 28], although a critical angle exists where the interaction is maximized [29]. Away from such angle, the Raman spectra of multi-layer graphene will not be very different from single-layer graphene. Section 3 of the supplementary information is referred for further explanations of the assignment made of stacking order to each Raman spectra.

One would expect to see the same variety of stacking order also for the Raman spectra of the 1 μm channel. Despite the proximity of the 10 μm and 1 μm regions, this is not exactly the case. Results for the 1 μm channel are shown in figure 4(c). Firstly, it is noticed that because of the presence of a well-defined wrinkle, the results are considerably noisier compared to the case of the 10 μm gap. Secondly, the intensity ratio (I(2D)/I(G), figure SI 3) is roughly 1 for all points, apart from point 3 where I(2D)/I(G) $=$ 0.47. This is similar to the value of (I(2D)/I (G) $=$ 0.37 found at point 2 of 10 μm channel. Both are therefore assigned to a twisted-angle stacking order.

Given both the value of the I(2D)/I(G) ratio close to unity and the apparent difference in stacking order recorded between the 1 μm and 10 μm gap areas, the conclusion must be that the wrinkle present in the smaller gap makes the topmost layer stand above the four-layer stack, and it is, therefore, the only one that is revealed optically by Raman spectroscopy. Any other difference between the 1 μm and 10 μm gap areas must be due to strain, which is expected to be higher in the latter compared to the former. Another important assertion to make here is that it is difficult to deconvolve the separate contributions of different layers because the wrinkle is

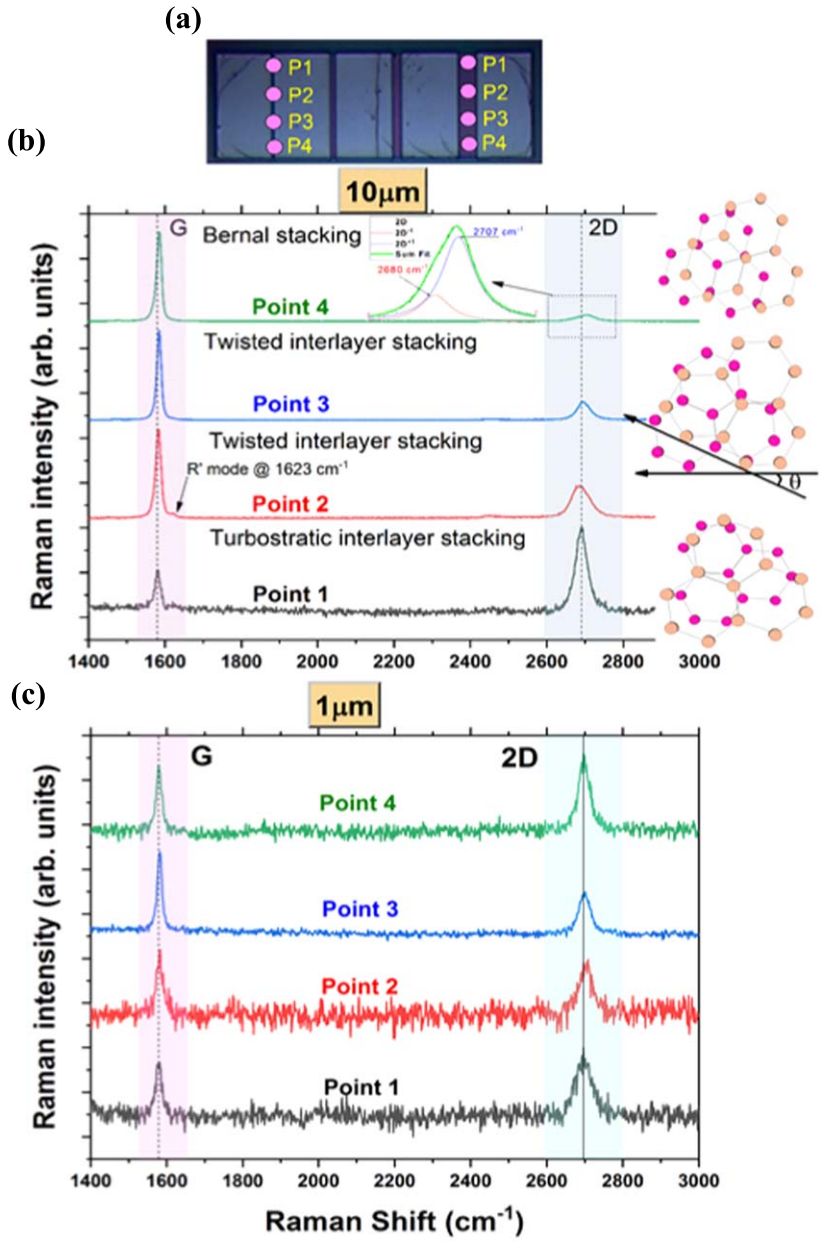

Figure 4. Raman spectra of the a) four points identified on the device; b) 10 μm and c) 1 μm channels.

formed from only a portion of the graphene that is present between the 1 μm channel. The optical signal from the unwrinkled bottom graphene layers is present in both 1 μm and 10 μm gaps, therefore, the I(2D)/I(G) could be expected to be similar for both the cases. However, I(2D)/I(G) for 1 μm was measured to be less than that for 10 μm channel. The actual reason for the low intensity ratio is not very clear here, however, with the given total laser spot size of 800 nm in diameter, it was difficult to align the laser spot and the reflected signal within 1 μm gap. This reduction in intensity ratio could be anticipated from the loss of optical signal scattered at the metal edges and/or the predomination of signal reflected off the wrinkled monolayer of graphene.

Figures SI 10 and SI 11 (supplementary information) show statistical data from several devices showing that the results presented in this section are repeatable and that the defect density is sufficiently low (inferred from the I(D)/I(G) ratio).

For the avoidance of doubt a hyperspectral analysis of a Raman map is shown in figure 5. Because of the small gap between the electrodes in the 1 μm channel, resolution is much better obtained in the Y direction along the channel than in the X direction across it. In the former, in fact, the 3 points measured cannot be deconvolved effectively for proximity issues and for the noise that the proximity of the electrodes produces. However one can still appreciate that the I(2D)/I(G) ratio is the clearest signature for the presence of a wrinkle in the middle of the gap between the contacts. Other quantities like G and 2D peak positions and the FWHM of the G peak, tend to provide information on the strain which appears to spatially extend further away from the wrinkled area,

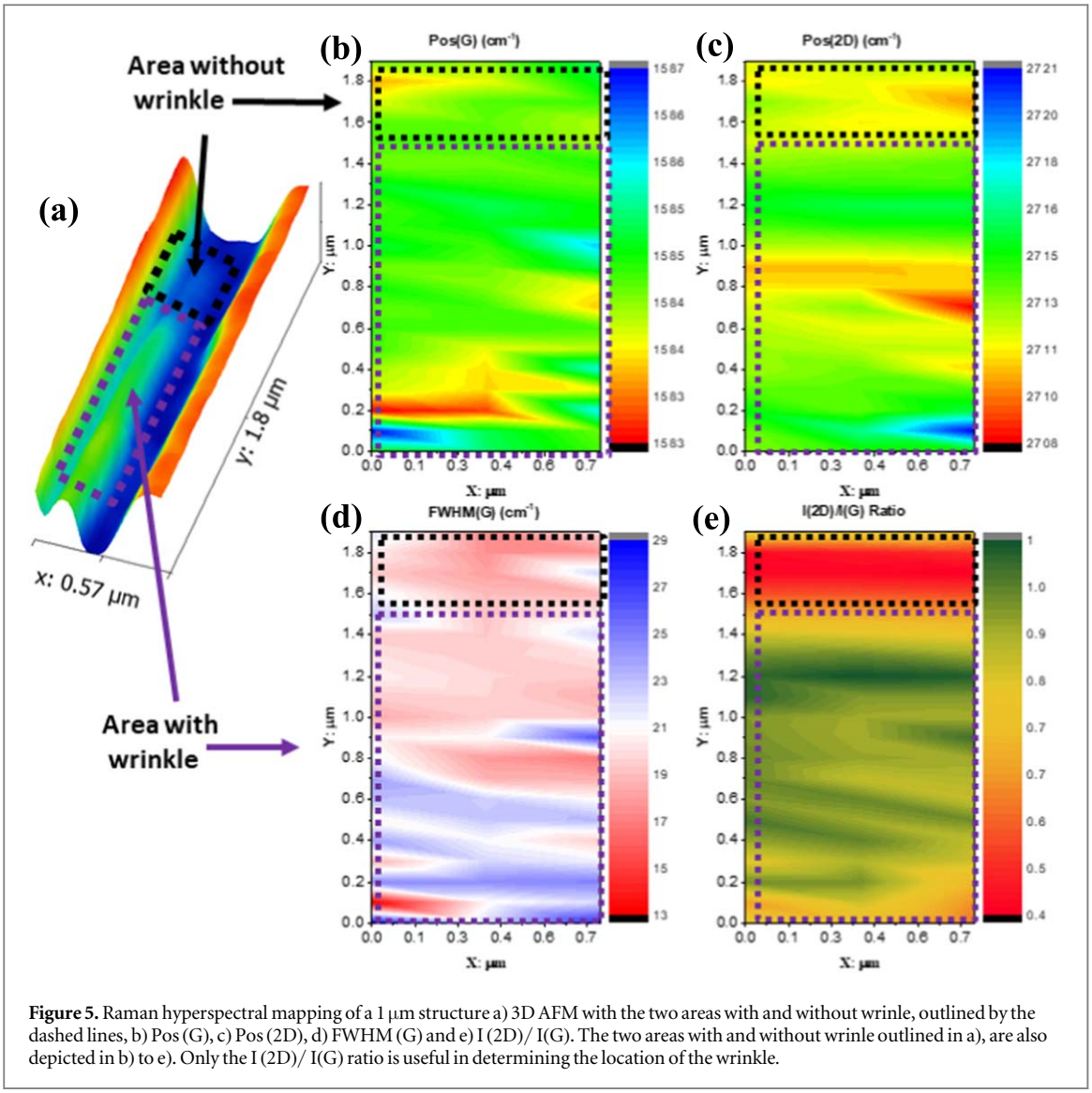

Figure 5. Raman hyperspectral mapping of a 1 µm structure a) 3D AFM with the two areas with and without wrinle, outlined by the dashed lines, b) Pos (G), c) Pos (2D), d) FWHM (G) and e) I (2D)/ I(G). The two areas with and without wrinle outlined in a), are also depicted in b) to e). Only the I (2D)/ I(G) ratio is useful in determining the location of the wrinkle.

towards the contacts. The next section will be devoted to identifying, quantifying and categorizing of strain discussed above.

3. Results and discussion

Here three different methods were used to an attempt to identify the signature of the presence of strain, quantify its amount, and finally determine the direction and type of 2D strain present around the wrinkles. This is achieved using AFM, polarized Raman and modelling.

3.1. Strain analysis through AFM

The amount of strain around the wrinkle that originated in the 1 μm channel is now estimated by concentrating on an area along a line (line 2) between the electrodes (figures 4(a) and (b)). The distance between the two edges of the electrodes L is estimated by the black line to be 0.6 μm (though the gap is nominally 1 μm, the shrinking of this feature being most likely associated with thermal stress), as shown in figure 6(a).

There are two possible interpretations for wrinkle formation (figure 7) and consequently distinct approaches in evaluating the strain. One view (see e.g. [10]) is that the wrinkle is akin to a 'bubble' forming as a result of a localized force under the graphene sheet (figure 7(a)). Alternatively, the wrinkle forms as a result of the graphene layer 'slipping' as a result of the metal contact exerting a uniaxial compressive force transverse to the direction longitudinal to the wrinkle (figure 7(a)). The main difference between the two models is that the 'bubble' formation results in a localized tensile strain, while the 'slip' model implies both compressive and tensile strain forming together. The former is consistent with modelling results [30]. In terms of modelling framework, the 'bubble' approach can be implemented as follows. Firstly, one estimates the height and width of the wrinkle,

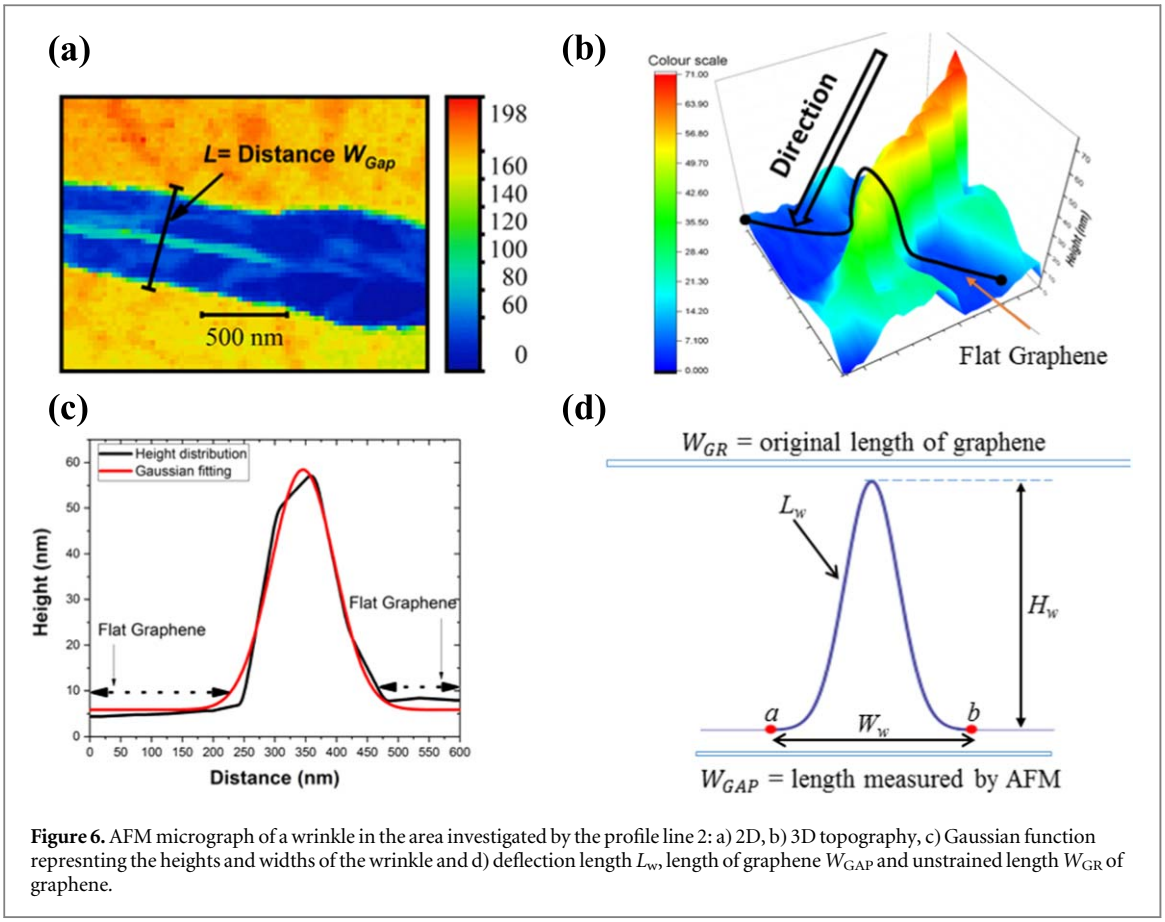

Figure 6. AFM micrograph of a wrinkle in the area investigated by the profile line 2: a) 2D, b) 3D topography, c) Gaussian function represnting the heights and widths of the wrinkle and d) deflection length L_w, length of graphene W_{GAP} and unstrained length W_{GR} of graphene.

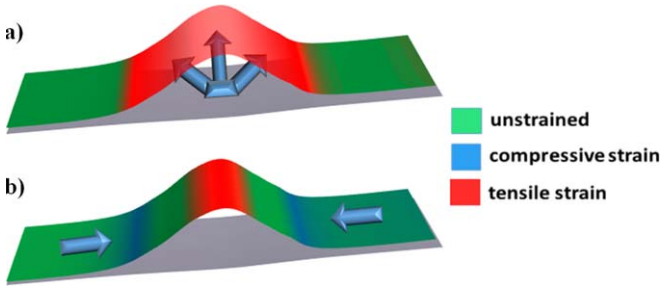

Figure 7. Expected strain distribution in a sheet of wrinkled graphene assuming a) a "bubble" caused by an isotropic force underneath the graphene layer, b) a uniaxial sliding of the graphene sheet.

using a Gaussian function to fit its curvature, as shown in figure 6(c). Secondly, to estimate the upper limit of the transverse strain ε_T present over the wrinkle the following expression can be used:

$$W_{GR} = W_{GAP} - W_W + L_W \tag{1}$$

$$L_W = \int_a^b \sqrt{1 + f'(x)}\, dx \tag{2}$$

$$\varepsilon_T = \frac{W_{GR} - W_{GAP}}{W_{GAP}} = \frac{L_W - W_W}{W_{GAP}} \tag{3}$$

where W_{GR} is the total length of the graphene between the metal contacts after the bubble is formed, W_{GAP} is the distance between the metal electrodes, W_w is the width of graphene that has become strained/deformed, L_w is the new length of the portion of graphene that has undergone deformation, and $f(x)$ is the Gaussian function that fits the wrinkle profile. The portion of unstrained graphene is described by the dark blue area in figure 6(a) where the graphene is assumed flat and not raised. By adding to W_{GAP} the length of the Gaussian profile of figure 6(d)), L_W (equation (2), where a and b are the start and end positions of the width of the wrinkle W_W and

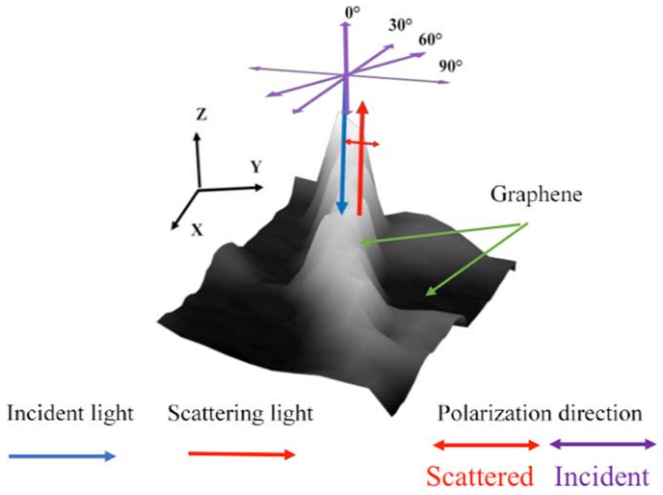

Figure 8. Schematic diagram for the polarized micro-Raman scattering representing directions of incidence and scattered beam off the wrinkles topgraphy.

$f'(x)$ is the first derivative of the fitted Gaussian function) and subtracting W_W, the new transverse length of the W_{GR} is obtained (equation (1)). The one-dimensional strain ε_T is then given by equation (3).

The range of longitudinal strain is found to be between 0.66% and 3.8% (tensile strain), with the wrinkle height varying between 20 nm and 53 nm, respectively. The average is 2.23% along the length of the wrinkle investigated. Unlike the 'bubble' model, where the strain is invariably tensile, the 'slip' model can locally yield both compressive and tensile strain, and requires a much more complex modelling framework.

Experimentally, it would be very unlikely that any measurement would be able to quantitatively determine the extent of both types of strain, due to spatial resolution limitations. Instead it is likely that an analog average of the local strains would be measured. If the average indicates that only compressive strain is present, then one can discard the 'bubble' model and assume that 'slipping' is the origin of the wrinkle formation. The converse however does not apply. If tensile strain is identified, it does not validate the 'bubble' approach, as it could just mean that the amount of tensile strain is larger than the amount of compressive strain. In the next paragraph we will show how polarized Raman spectroscopy can help discriminate between the two cases.

3.2. Strain analysis through polarized Raman spectroscopy

Because strain creates subpeaks within the 2D and G Raman peaks, polarized Raman [31, 32], where different subpeaks become redshifted and blueshifted at the same time, can be used to determine the directions where the strain is highest. Figure 8 depicts the incident and scattered polarized Raman radiation in relation to the measured rippled graphene. Polarized Raman measurements were performed, with the angle of the incident polarized light in the z-direction (one-sided blue arrow) from 0° to 90° (two-sided purple arrow in the x-direction). The angle of the incident laser in respect of the graphene surface (one-sided green arrow) was changed using a circular rotating stage, which provides 360° rotation. The backscattered laser beam in the z-direction (one-sided red arrow) is collected after scattering off the graphene. By using a spectrum analyzer, the collected light is polarized perpendicularly (two-sided red arrow on y-direction) with regard to the incident polarized light.

Figure 9 shows the polarized Raman spectrum at location 1 and 3 of the 1 μm channel that was identified previously. The Raman spectra of the other locations (2 and 4) are displayed in the supplementary information (figure SI 4). The left and right columns are the data for the 2D and G modes, respectively.

Both Raman modes depend on the angle of the incident laser beam. The single filled peaks (olive and blue) at the various degrees of the incident beam, can be fitted by a single Lorentzian function. No appreciable difference between the subpeaks can be directly measured at location 3, presumably because the amount of stress is low. However at location 1, using a triple Lorentzian fit, up-shifted/down-shifted sub-peaks G^+;$2D^+$/G^-;$2D^-$ (in respect of the peaks of stress-free graphene, G^0;$2D^0$) are observed, evidenced as the blue and red filled curve. The G mode at 30° of location 3 is, however, comprised of two subpeaks (G^+/G^-) that can be fitted with only two Lorentzian functions. It is proposed that when a triple Lorentzian fit is required, it is evidence that there is a mixture of strained and unstrained regions contributing to the spectra, while the double Lorentzian arises from a fully-strained region.

Furthermore, looking at location 1, while the spectral profile of at 0° is symmetric, as the degree of polarized incident light increases the spectral shape begins to lose its symmetry due to the emergence of sub-peaks,

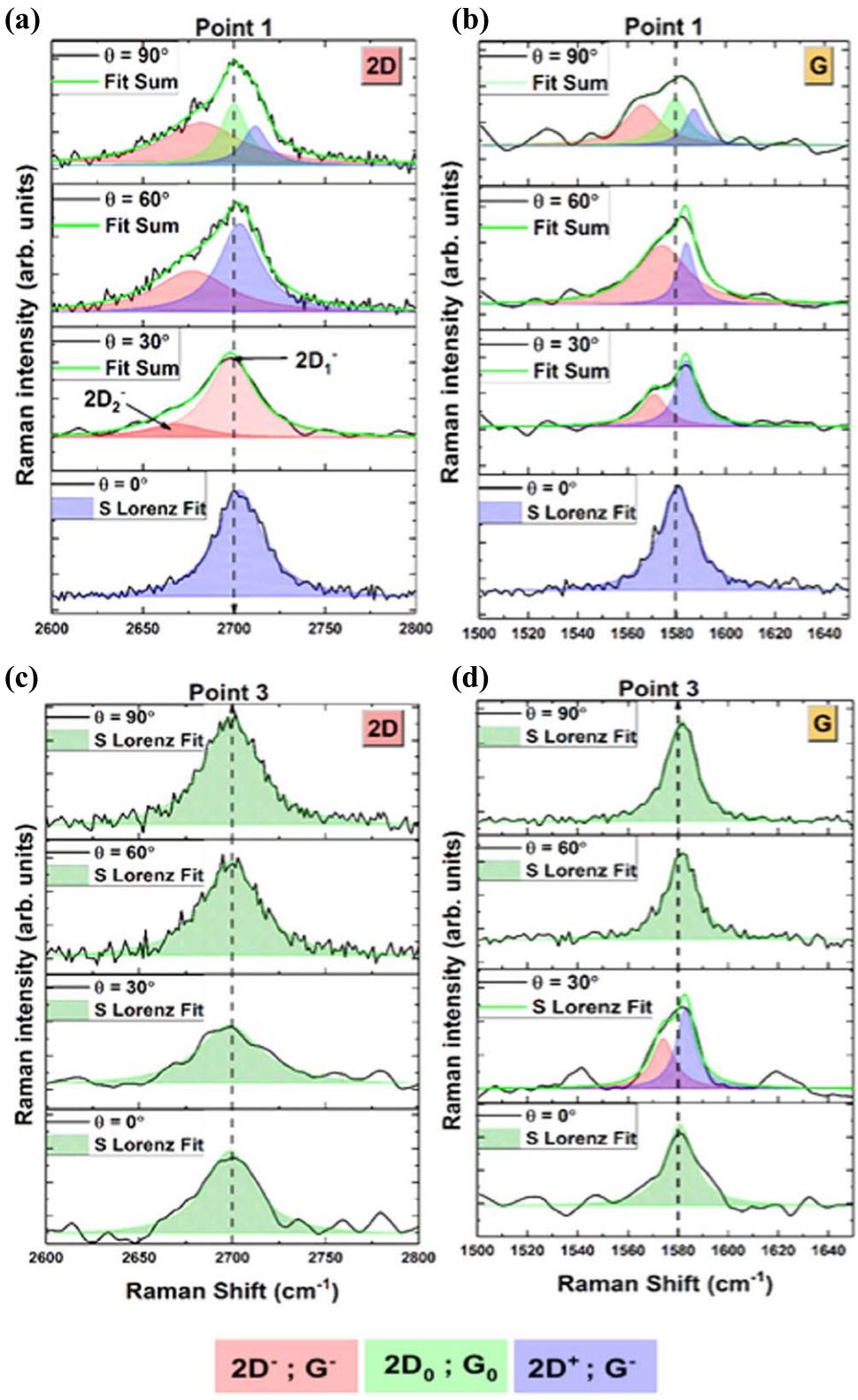

Figure 9. Polarized Raman spectra for the a) 2D and the b) G mode at location 1 and the c) 2D and d) G mode at location 3.

eventually becoming asymmetric. Also, the change in FWHM of the overall spectral profile depends on the number (and FWHM) of generated sub-peaks, which in turn depends on the amount of stress. The highest FWHM of the spectral profile of both Raman modes can be found at 60° to the polarized incident light. As the FWHM increases/decreases as a consequence of the subpeaks becoming red/blueshifted, an increase in a particular direction means that this is the direction where the strain is largest. Table SI1 (supplementary information) summarises the peak positions, sub-peak positions, and FWHMs of the Raman modes at locations 1 and 3 at different polarization angles of the incident laser beam.

So far no attempt was made to identify the type of strain responsible for the observed spectral properties. It is well established that when graphene is under the influence of high uniaxial tensile (compressive) stress, both the G^-;$2D^-$ (G^+;$2D^+$), though spectrally separated, should redshift (blueshift) compared to the zero strain frequency of the G^0;$2D^0$ peaks [25, 32]. This is not what appears to happen in figure 9 (and table SI1, supplementary information). At 30° of incident light, the strain induced sub-peaks ($2D_1^-$ and $2D_2^-$) at point 1 are redshifted in relation to ($2D^0$), but the subpeaks G^+;$2D^+$ are blueshifted compared to G^0;$2D^0$. This suggests that while tensile strain is present, the tension generated in graphene cannot be assigned directly to uniaxial strain and that a different type of strain must be responsible [27]. It is further duscussed in the modelling results in section 4.3.

From the polarized Raman measurements, the peak shifts of the G and 2D modes can be used to determine the amount of strain generated at the selected four points. The widely-used equation given by Mohiuddin *et al* [32] is used here in this study, which links the shift of the G:2D mode frequency, $\Delta\mathrm{Pos(G:\ 2D)}^S$ to the peak position of the G:2D mode at zero strain, the position itself $\mathrm{Pos(G:\ 2D)}^0$, due to the strain components along two orthogonal directions is given in equation (4):

$$\Delta\mathrm{Pos(G:\ 2D)}^s_{\pm} = -\mathrm{Pos(G:\ 2D)}^0\gamma_{\mathrm{G:2D}}(\varepsilon_l + \varepsilon_t)(1-\nu) \pm \frac{1}{2}\mathrm{Pos(G:\ 2D)}^0\beta_{\mathrm{G:2D}}(\varepsilon_l - \varepsilon_t)(1+\nu), \quad (4)$$

where, ε_l and ε_t are the longitudinal and transverse component of the strain. $\beta_{\mathrm{G:2D}}$ the shear deformation potential. The experimental and theoretical value of the shear deformation potential is 0.99 [32]. The quantities $(\varepsilon_l - \varepsilon_t)$ and $(\varepsilon_l + \varepsilon_t)$ are the shear and hydrostatic components of the applied strain, respectively. The quantity $\gamma_{\mathrm{G:2D}}$ is the Grüneisen parameter. The value of $\gamma_{\mathrm{G:2D}}$ for the G (2D) mode is 1.99 [32] (1.24 [33]). The quantity ν is the Poisson's ratio, which ranges from 0.33 for a good contact between graphene and its substrate to 0.13 for suspended graphene [32]. In this study of curved graphene, 0.16 was chosen [34], which is the experimental value of graphite.

From figures 8(a), (b) for a polarized direction of 90°, the unstrained peak position of the G^0 ($2D^0$) is determined to be 1580 cm^{-1} (2699 cm^{-1}), which is in excellent agreement with other studies who used incident laser energy of 2.41 eV [21].

The dependence on strain for the 2D and G modes of locations 1, 2 and 4 for the four polarization angles are summarised in table SI2 in supplementary information.

For point 1, the maximum (minimum) value of tensile strain of the 2D mode is 2.32% (0.036%) at a polarization angle of 30°, with an average strain of about 1.76%. The maximum (minimum) value of compressive strain is −0.26% (−0.69%) at a polarization angle of 90° (60°) with an average strain of about −0.14%. For the G mode, the average produced tensile (compression) is 0.49% (−0.13%). At point 2, however, we find that the average of tensile (compressive) strain of the 2D mode is 0.60% (−0.04%), which is less than what is evaluated for point 1. The average of tensile strain is observed for the G mode, which is about 0.09%. Last but not least, for point 4 the average of tensile strain of the 2D mode is (1.63%) which is very close to that of the point 1, but the average value of the compression strain is −0.01%. For the G mode, the average of tensile (compressive) strain generated is 0.18% (−0.03%). We can conclude that in comparison the strain influences more the 2D mode compared to the G mode, making changes in the 2D mode a better probe for detecting even small amount of strain in graphene, consistent with previous studies [35].

It is also noted that rather than the strain being largest in the longitudinal or transverse direction to the wrinkle, it's maximum is at 30° instead. This is due to the fact that the strain induced by the electrodes, produces a deformation of the graphene, which turns into a wrinkle, and where a local (internal) strain is produced which does not need to align itself to the original strain that induces the wrinkle. In terms of magnitude, the average strain values obtained from Raman spectroscopy are similar to those obtained from the AFM data. However the fact that a mixture of compressive and tensile strains could be identified, suggests that the 'bubble' model should be discarded in favour of the 'slip' model. Which implies wrinkles do form as a result of uniaxial strain created by the metallization step during fabrication.

Having obtained quantitative information on both the magnitude, type and direction of the strain present around the graphene wrinkles, atomistic modelling is further used to confirm the effect such strain has on the local bandstructure.

3.3. Density functional theory modelling

In the modelling, four kinds of stress were applied to the hexagonal structure of graphene: uniaxial tensile, uniaxial compressive, hydrostatic tensile and biaxial, as shown in figure SI 5 (supplementary information).

The computational results were obtained using the simulation software package CASTEP [36, 37], a density functional theory package that allows for geometry optimization and electronic structure calculations. Further details are given in section 4 (supplementary information). The calculations performed confirm that when the

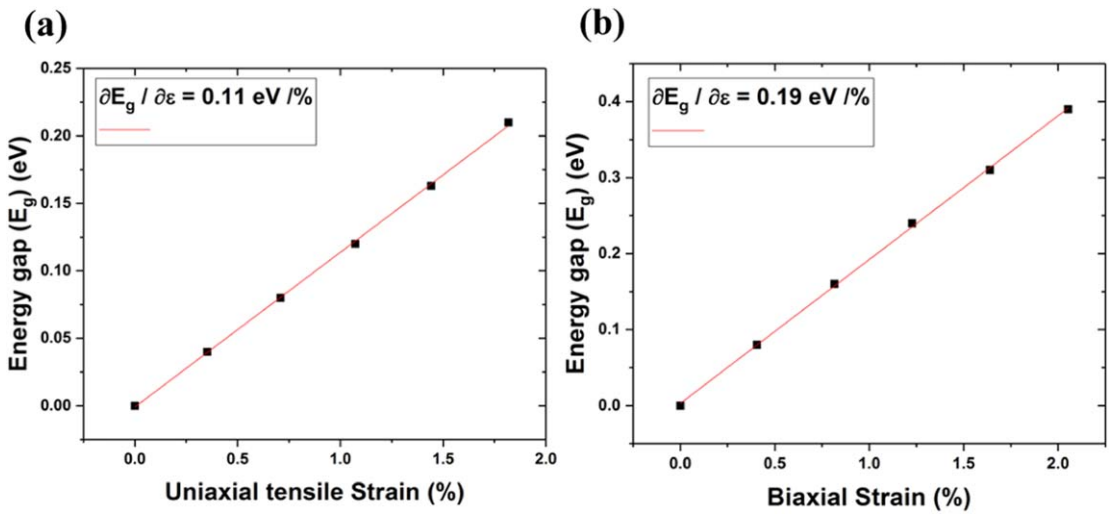

Figure 10. Energy gap of graphene as a function of; a) uniaxial tensile and b) biaxial strain.

band structure of graphene undergoes uniaxial and biaxial deformation, a fairly-large energy gap can be achieved, the value of which depends roughly linearly on the amount of strain as shown in figure 10. In the case of the biaxial stress, the calculated bandgap rate of change per percentage of strain is 0.19 eV % (figure 10(a)), a value larger (almost double) than the rate of change for uniaxial stress, 0.11 eV % (figure 9(b)). This means that a biaxial deformation of only 2% would result in a bandgap of 380 meV, similar to that of the semiconductor InAs at room temperature.

To model the polarized Raman measurements, the spectra were computed based on density functional perturbation theory (DFPT) and using the dynamical matrix approach to model non-resonance Raman processes. In addition, Raman intensities of each mode were computed by finding the modification in polarizability with respect to the excitation of a phonon mode under an external perturbation (such as due to photons). More information about computing Raman intensities using the CASTEP code can be found in the work published by Porezag and Pedersen [38]. Further details are given in section 4 (supplementary information).

The results are presented in figure 11 showing the G mode dependence on (a) uniaxial tensile (b) uniaxial compressive (c) hydrostatic (d) biaxial strain. While hydrostatic strain does not lead to any redshift/blueshift of the G^-/G^+ subbands, both uniaxial tensile and compressive strain exhibit a combined redshift/blueshift of both subbands compared to the G^0 band. This is despite the two subbands red/blue shifting in respect of each other as their separation increases with strain. Only in the case of biaxial strain, there is no overall redshift/blueshift, but rather the G^-/G^+ subbands blueshifts/redshift individually in respect of G^0, precisely as observed experimentally for the G band (figure 9).

This allows to conclude that the strain present along the ripple is of the biaxial type, and since the biaxial strain is able to produce a bandgap opening, it is asserted that the wrinkle leads to a semiconducting graphene region in the middle of two conductive graphene regions. This also confirms our earlier work [30], where the biaxial strain in warped graphene was shown to be a viable pathway to bandgap opening in substrate-less graphene films.

The energy gap can be calculated using DFT (even though these are usually underestimated [39]), and the energy rate of change per unit of the strain rate is given in figure 10(b). Typical values of the strain inferred from the Raman data are much smaller than those determined from AFM, around 2%, which would lead to a band gap of 0.38 eV, which is still rather sizeable.

4. Conclusions

CVD Graphene was grown on copper and repeatedly transferred onto a SiO_2 substrate to form a four-layer graphene stack on which two gold electrodes were evaporated. Varying gaps from 1 μm to 10 μm were obtained. AFM shows that while in the area with a 10 μm gap there are relatively small height variations, in the 1 μm gap area, these height variations appear to coalesce into a large regular wrinkle longitudinal to the electrodes, roughly in the middle of the gap. Analyzing the Raman spectra in the 10 μm gap region shows that the four layers of graphene are stacked in a variety of arrangements, long and short-range ordered. The absence of evidence of the

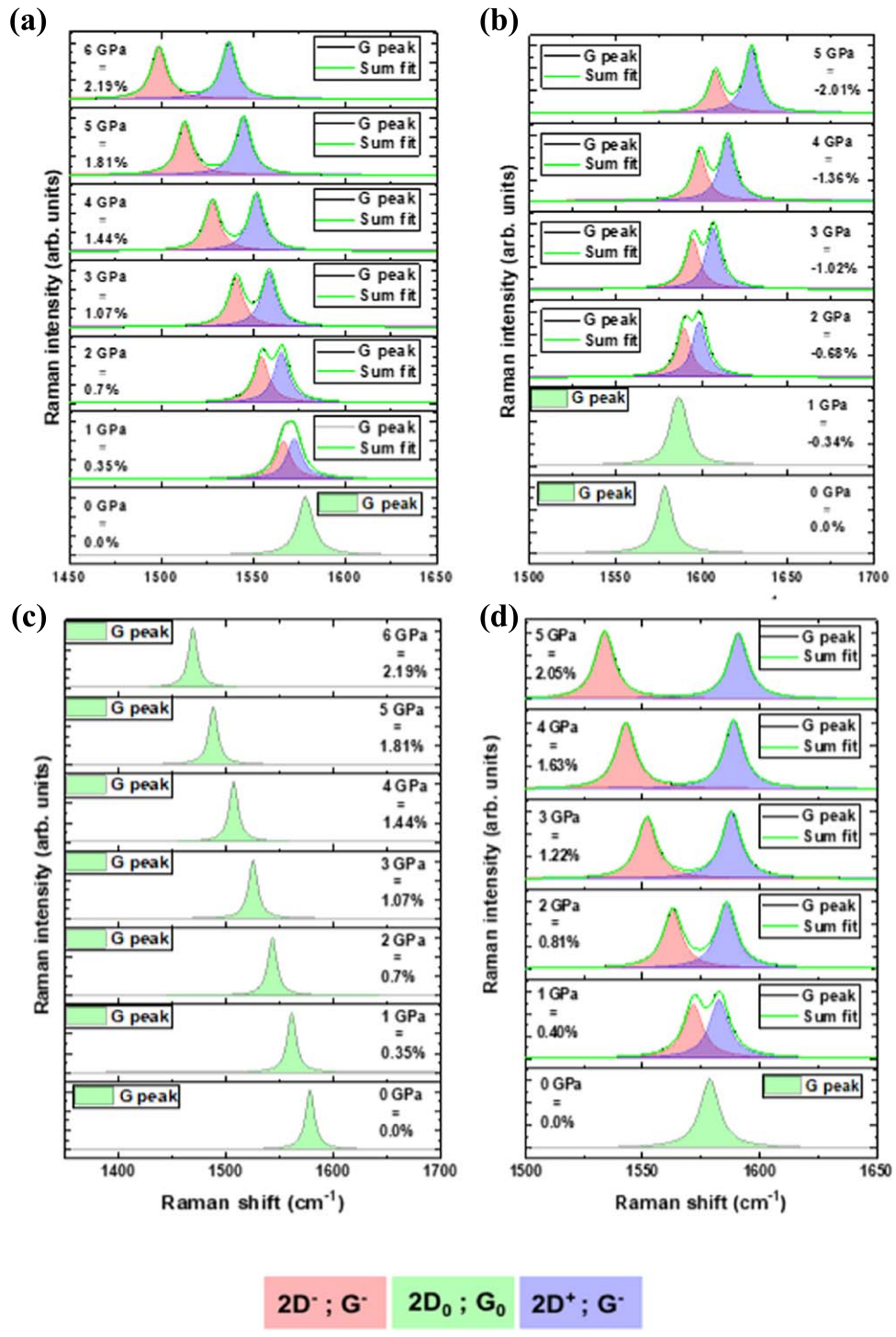

Figure 11. Calculated Raman spectra for the G mode under the influence of a) uniaxial tensile, b) uniaxial compressive, c) hydrostatic tensile and d) biaxial stress.

same for the 1 μm gap region, suggests that the topmost layer of graphene is lifted from the other three layers, and react more to strain created by the metal electrodes than the graphene layers underneath. From the optical point of view, the topmost layer can be probed independently from the rest of the graphene stack, and essentially behaves like a strained graphene monolayer.

Three different approaches were used to identify the amount, direction and type of strain along the wrinkle, using atomic force microscopy, polarized Raman and DFT modelling. It is found that while the electrodes impose an average compressive strain, the strain determined by Raman spectroscopy is of the order of 2.3%, tensile, aligned at 30° to the wrinkle and of the biaxial type. This is unsurprising as the formation of a wrinkle produces a local strain which is a mixture of different types and values of strain that cannot be assigned to a specific angle. Modelling shows that such biaxial strain would lead to a bandgap of the order of 0.4 eV.

Since graphene is normally a zero bandgap material, applications as an electronic material have often been considered to be limited. However, the approach presented in this work show that a region of graphene with a controllable bandgap similar to a narrow gap semiconductor can be regularly formed using lithographic techniques. This shows great promise for being exploited as a basis for fabrication of graphene electronic devices.

Acknowledgments

O M Dawood is grateful for the support of the Ministry of Higher Education and Scientific Research (MOHESR), Iraq.

ORCID iDs

Omar M Dawood https://orcid.org/0000-0003-3655-0656
Hong-Yeol Kim https://orcid.org/0000-0001-7139-0884
Max A Migliorato https://orcid.org/0000-0001-8394-7854

References

[1] Chen X P, Zhang L L and Chen S S 2015 Large area CVD growth of graphene *Synthetic Met* **210** 95–108
[2] Lee Y, Bae S, Jang H, Jang S, Zhu S E, Sim S H, Song Y I, Hong B H and Ahn J H 2010 Wafer-scale synthesis and transfer of graphene films *Nano Lett.* **10** 490–3
[3] Wood J D, Schmucker S W, Lyons A S, Pop E and Lyding J W 2011 Effects of polycrystalline Cu substrate on graphene growth by chemical vapor deposition *Nano Lett.* **11** 4547–54
[4] Zhao L, Rim K T, Zhou H, He R, Heinz T F, Pinczuk A, Flynn G W and Pasupathy A N 2011 Influence of copper crystal surface on the CVD growth of large area monolayer graphene *Solid State Commun.* **151** 509–13
[5] Bae S, Kim H, Lee Y, Xu X, Park J-S, Zheng Y, Balakrishnan J, Lei T, Kim H R and Song Y I 2010 Roll-to-roll production of 30-inch graphene films for transparent electrodes *Nat. Nanotechnol.* **5** 574
[6] Wang G, Kim Y, Choe M, Kim T W and Lee T 2011 A new approach for molecular electronic junctions with a multilayer graphene electrode *Adv. Mater.* **23** 755 -+
[7] Sui Y and Appenzeller J 2009 Screening and interlayer coupling in multilayer graphene field-effect transistors *Nano Lett.* **9** 2973–7
[8] Zhu W, Low T, Perebeinos V, Bol A A, Zhu Y, Yan H, Tersoff J and Avouris P 2012 Structure and electronic transport in graphene wrinkles *Nano Lett.* **12** 3431–6
[9] Jariwala D, Srivastava A and Ajayan P M 2011 Graphene synthesis and band gap opening *J. Nanosci. Nanotechnol.* **11** 6621–41
[10] Wang W, Yang S and Wang A 2017 Observation of the unexpected morphology of graphene wrinkle on copper substrate *Sci. Rep.* **7** 8244
[11] Liu N, Pan Z, Fu L, Zhang C, Dai B and Liu Z 2011 The origin of wrinkles on transferred graphene *Nano Res.* **4** 996
[12] Li Z, Kinloch I A, Young R J, Novoselov K S, Anagnostopoulos G, Parthenios J, Galiotis C, Papagelis K, Lu C Y and Britnell L 2015 Deformation of wrinkled graphene *ACS Nano* **9** 3917–25
[13] Deng S K and Berry V 2016 Wrinkled, rippled and crumpled graphene: an overview of formation mechanism, electronic properties, and applications *Mater. Today* **19** 197–212
[14] Yu S U, Park B, Cho Y, Hyun S, Kim J K and Kim K S 2014 Simultaneous visualization of graphene grain boundaries and wrinkles with structural information by gold deposition *ACS Nano* **8** 8662–8
[15] Bissett M A, Tsuji M and Ago H 2014 Strain engineering the properties of graphene and other two-dimensional crystals *Phys. Chem. Chem. Phys.* **16** 11124–38
[16] Kim H-Y, Dawood O M, Monteverde U, Sexton J, Li Z, Britnell L, Migliorato M A, Young R J and Missous M 2016 Multilayer stacking and metal deposition effects on large area graphene on GaAs *Carbon* **96** 83–90
[17] Shioya H, Craciun M F, Russo S, Yamamoto M and Tarucha S 2014 Straining graphene using thin film shrinkage methods *Nano Lett.* **14** 1158–63
[18] Lindahl N, Midtvedt D, Svensson J, Nerushev O A, Lindvall N, Isacsson A and Campbell E E 2012 Determination of the bending rigidity of graphene via electrostatic actuation of buckled membranes *Nano Lett.* **12** 3526–31
[19] Chen X M, Yi C L and Ke C H 2015 Bending stiffness and interlayer shear modulus of few-layer graphene *Appl. Phys. Lett.* **106** 101907
[20] Cui Z and Guo J G 2016 Theoretical investigations of the interfacial sliding and buckling of graphene on a flexible substrate *AIP Adv.* **6** 125110
[21] Ferrari A C *et al* 2006 Raman spectrum of graphene and graphene layers *Phys. Rev. Lett.* **97** 187401
[22] Das A, Chakraborty B and Sood A 2008 Raman spectroscopy of graphene on different substrates and influence of defects *Bull. Mater. Sci.* **31** 579–84
[23] Casiraghi C, Pisana S, Novoselov K, Geim A and Ferrari A 2007 Raman fingerprint of charged impurities in graphene *Appl. Phys. Lett.* **91** 233108
[24] Bruna M, Ott A K, Ijas M, Yoon D, Sassi U and Ferrari A C 2014 Doping dependence of the Raman spectrum of defected graphene *ACS Nano* **8** 7432–41
[25] Huang M, Yan H, Chen C, Song D, Heinz T F and Hone J 2009 Phonon softening and crystallographic orientation of strained graphene studied by Raman spectroscopy *Proc. Natl Acad. Sci. USA* **106** 7304–8
[26] Huang C W, Lin B J, Lin H Y, Huang C H, Shih F Y, Wang W H, Liu C Y and Chui H C 2012 Observation of strain effect on the suspended graphene by polarized Raman spectroscopy *Nanoscale Res. Lett.* **7** 533
[27] Huang C W, Shiue R J, Chui H C, Wang W H, Wang J K, Tzeng Y and Liu C Y 2013 Revealing anisotropic strain in exfoliated graphene by polarized Raman spectroscopy *Nanoscale* **5** 9626–32
[28] Karamat S, Sonusen S, Celik U, Uysalli Y, Ozgonul E and Oral A 2015 Synthesis of few layer single crystal graphene grains on platinum by chemical vapour deposition *Prog Nat Sci-Mater* **25** 291–9

[29] Kim K, Coh S, Tan L Z, Regan W, Yuk J M, Chatterjee E, Crommie M F, Cohen M L, Louie S G and Zettl A 2012 Raman spectroscopy study of rotated double-layer graphene: misorientation-angle dependence of electronic structure *Phys. Rev. Lett.* **108** 246103
[30] Monteverde U, Pal J, Migliorato M, Missous M, Bangert U, Zan R, Kashtiban R and Powell D 2015 Under pressure: control of strain, phonons and bandgap opening in rippled graphene *Carbon* **91** 266–74
[31] Yoon D, Son Y W and Cheong H 2011 Strain-dependent splitting of the double-resonance Raman scattering band in graphene *Phys. Rev. Lett.* **106** 155502
[32] Mohiuddin T, Lombardo A, Nair R, Bonetti A, Savini G, Jalil R, Bonini N, Basko D, Galiotis C and Marzari N 2009 Uniaxial strain in graphene by Raman spectroscopy: G peak splitting, Grüneisen parameters, and sample orientation *Phys. Rev.* B **79** 205433
[33] Reich S, Jantoljak H and Thomsen C 2000 Shear strain in carbon nanotubes under hydrostatic pressure *Phys. Rev.* B **61** 13389–92
[34] Gauster W B and Fritz I J 1974 Elastic-constants of compression-annealed pyrolytic-graphite as a function of pressure to 20 Kbar *Ieee T Son Ultrason* **Su21** 62 -
[35] Frank O, Mohr M, Maultzsch J, Thomsen C, Riaz I, Jalil R, Novoselov K S, Tsoukleri G, Parthenios J and Papagelis K 2011 Raman 2D-band splitting in graphene: theory and experiment *ACS Nano* **5** 2231–9
[36] Milman V, Refson K, Clark S J, Pickard C J, Yates J R, Gao S P, Hasnip P J, Probert M I J, Perlov A and Segall M D 2010 Electron and vibrational spectroscopies using DFT, plane waves and pseudopotentials: CASTEP implementation *J Mol Struc-Theochem* **954** 22–35
[37] Clark S J, Segall M D, Pickard C J, Hasnip P J, Probert M I, Refson K and Payne M C 2005 First principles methods using CASTEP *Zeitschrift für Kristallographie-Crystalline Materials* **220** 567–70
[38] Porezag D and Pederson M R 1996 Infrared intensities and Raman-scattering activities within density-functional theory *Phys. Rev.* B **54** 7830–6
[39] Perdew J P and Levy M 1983 Physical content of the exact kohn-sham orbital energies - band-gaps and derivative discontinuities *Phys. Rev. Lett.* **51** 1884–7